PAPER

Check for updates

Tristate ferroelectric memory effect attained by tailoring the ferroelectric behavior in $Bi_{1/2}$ $(Na_{0.8}K_{0.2})_{1/2}TiO_3$ with Eu doping†

Yang Hu,[a] Huazhang Zhang,[ab] Jing Zhou,[ac] Jie Shen,[a] Binbin Chen,[a] Ang Li[a] and Wen Chen ![ORCID] *[a]

The ferroelectric behavior of $Bi_{1/2}(Na_{0.8}K_{0.2})_{1/2}TiO_3$ has been tailored by Eu^{3+} doping and the intermediate relaxor state is utilized for tristate ferroelectric memory effect. As Eu^{3+} content increases, the local structural disorder tends to get enhanced and the stability of ferroelectric order gets weakened. The disruption effect of Eu^{3+} is manifested structurally in XRD and PL spectra, and electrically in the ferroelectric, dielectric and piezoelectric properties. We found that the BNKT:3.0%Eu which owns a relaxor state under electrical cycle would be suitable for tristate ferroelectric memory, where two ferroelectric states and the relaxor state are respectively served as the "±1" and "0" memory states. We designed the verification experiments, and the results show good feasibility and stability. Moreover, it is innovative using PL spectra of Eu^{3+} to understand the structural changes related to different memory states, owing to its sensitivity to local structural symmetry. It also implies the possibility for non-destructive optical readout.

1 Introduction

With the increasing concern for the earth environment and human health, it is urgent to explore lead-free ferroelectric materials with comparable performance to their lead-containing counterparts.[1–3] Among many lead-free materials, the $Bi_{1/2}Na_{1/2}TiO_3$ (BNT)-based ferroelectric, owing to the Bi^{3+} cation with similar electronic structure to that of Pb^{2+}, is likely to induce large spontaneous polarization and thus considered as a promising candidate.[4] Moreover, the A-site disorder in the BNT-based ferroelectrics gives rise to the presence of polar nanoregions (PNRs), which have an important impact on the phase, polarization, and relaxor ferroelectric characteristics.[5,6] Based on this, a variety of applications ranging from piezo-electricity,[7] electric field-induced strains,[8] electro-caloricity,[9] and dielectric energy storage[10] to the newly developed oxygen ion conductivity,[11] piezo-photoluminescence,[12] and multistate ferroelectric memory[13] have been proposed by the researchers.

For the BNT-based materials, it is crucial to tailor the relaxor ferroelectric behavior, because different functional applications require different relaxor ferroelectric behavior. For instance, the

[a]State Key Laboratory of Advanced Technology for Materials Synthesis and Processing, School of Materials Science and Engineering, Wuhan University of Technology, Wuhan 430070, P. R. China. E-mail: chenw@whut.edu.cn

[b]Department of Physics, School of Sciences, Wuhan University of Technology, Wuhan 430070, P. R. China

[c]Sanya Science and Education Innovation Park of Wuhan University of Technology, Sanya 572025, P. R. China

† Electronic supplementary information (ESI) available. See DOI: https://doi.org/10.1039/d2ra08232b

BNT-based ceramics behaving as normal ferroelectrics with square *P–E* loop and large remnant polarization are usually expected to have a large piezoelectric constant and beneficial for piezoelectric applications.[14] In contrast, the BNT-based materials for dielectric energy storage require slim *P–E* loops where the ferroelectric feature is largely suppressed, so as to achieve high energy storage capacity and efficiency.[15] If the electro-caloric effect or the electric field-induced strains are considered, the ferroelectricity in the materials needs to be disrupted but to a moderate level, so as to make use of the transitions between relaxor and ferroelectric states when electric field is applied.[16] In order to customize BNT-based materials for particular applications and optimize the performance, various modification strategies have been developed, including doping,[17,18] forming solid solutions or composites with ferroelectric and non-ferroelectric components,[19–21] *etc.*

Rare-earth element doping, as an effective strategy of tailoring the properties of ferroelectric perovskites, has attracted much attention in recent years. According to the similarity in ionic radii, the rare-earth ions are generally expected to occupy the A-site in the ABO_3 lattice of lead- or bismuth-based perovskites such as $Pb(Zr,Ti)O_3$, BNT, *etc.* Li *et al.* found that the local structural heterogeneity introduced by rare-earth doping significantly enhances the piezoelectricity for relaxor ferroelectrics.[22,23] Besides, owing to the unique electron structure and photoluminescence property of rare-earth ions, such as Pr^{3+}, Eu^{3+} and Sm^{3+}, when incorporating into the BNTs, they could alter the relaxor ferroelectric behavior and in the meantime render the crystal to have fascinating optical properties, which provides more potential in multifunctional applications in sensors,

Paper

memories and optoelectronic devices.[12,24,25] According to the Judd–Ofelt theory, the luminescent properties of rare-earth ions are also strongly influenced by the local symmetry of the host crystal,[26,27] therefore the dopant rare-earth ions can be used as probes to monitor local structural changes.[28,29] This method has particular advantages in BNT-based systems because the Bi^{3+} can serve as a sensitizer and activator,[30] and the low phonon energy of BNT further makes it an outstanding luminescent matrix.[31]

In our previous work, we proposed a new functionality of the BNT-based relaxor ferroelectrics: the tristate ferroelectric memory effect, which could efficiently increase the storage density of ferroelectric memory devices, and we have previously verified in the B-site Fe, Nb co-doped $Bi_{1/2}(Na_{0.8}K_{0.2})_{1/2}TiO_3$ (BNKT).[13] We believe that the principle of the tristate ferroelectric memory effect is universal, *i.e.* it only depends on the particular ferroelectric behavior in which the polarization reversal is accomplished in two steps, while the material modification methods to achieve such ferroelectric behavior should be diversiform. However, this point of view is still a conjecture, which requires more supports from experiment. To date, it is unclear whether the tristate ferroelectric memory effect can be realized in A-site modified BNTs. Therefore, in this work we performed A-site modification of BNKT by the rare-earth element Eu, and investigated the Eu^{3+} doping effect and the potential of tristate ferroelectric memory effect. The introduction of Eu^{3+} is multi-faceted: On one hand it is used to tailor the ferroelectric properties of BNKT. On the other hand, it can impart the fluorescent properties to crystal. Benefit from the sensitivity to local structural symmetry, the fluorescent property not only provides a way to understand the structural changes related to the switching of the memory states, but also implies the potential for non-destructive optical readout.

2 Experimental

Eu^{3+} doped BNKT ceramic samples were prepared *via* a solid-state synthesis route. The nominal compositions of the samples are $(Bi_{1-x}Eu_x)_{1/2}(Na_{0.8}K_{0.2})_{1/2}TiO_3$ (abbreviated as BNKT:xEu), where $x = 0.0\%, 1.0\%, 2.0\%, 3.0\%, 4.0\%$ and 5.0%. Analytical grade Na_2CO_3 (99.8%, Sinopharm, China), K_2CO_3 (99.0%, Sinopharm, China), Bi_2O_3 (AR, Sinopharm, China), TiO_2 (99.0%, Aladdin, China), and Eu_2O_3 (99.9%, Sinopharm, China) powders were used as the starting materials. Amounts of 1.0% excess Bi, Na, and K were added to compensate the volatility. The mixture of starting materials was ball-milled in ethanol for 12 hours and dried overnight. The dried raw materials were calcined at 880 °C for 2 h, and then pressed into disks using polyvinyl acetate as an adhesive under a uniaxial pressure of 150 MPa. The disk-shaped samples were sintered at 1180 °C for 2 h. Silver electrodes were coated on both sides of the samples for electrical measurements. The poled samples were accessional treated by applying DC electric field of 5.0 kV mm^{-1} for 30 minutes at room temperature in a silicone oil bath.

Bulk density of the samples was measured by Archimedes' method. The microstructure and morphology were observed by field-emission scanning electron microscope (FESEM, Zeiss Ultra Plus, Germany), and the compositional analysis was conducted

with the attached X-ray diffractometer (EDS, X-Max 50, Oxford, UK) operated at acceleration voltage of 15 kV. The phase structure was examined by an X-ray diffractometer (XRD, D/max-2500H, Rigaku, Japan) operated at 40 kV and 150 mA, with a CuK_α radiation. The photoluminescent (PL) spectra were measured by the fluorescence spectrophotometer (FL3-22, Jobin Yvon, France). The final compositions of the synthesized samples were quantitively characterized by inductive coupled plasma emission spectrometer (ICP, Prodigy7, LEEMAN LABS, USA) and Atomic Absorption Spectrum (AAS, CONTRAA-700, Analytik Jena AG, Germany). The chemical states of the material were identified from X-ray photoelectron spectra (XPS, ESCALAB 250Xi, Thermo Fisher, USA). The measurement of polarization–electric field (P–E) hysteresis loops and the write/read tests for the memory property were conducted on a ferroelectric tester (Precision Workstation, Radiant Technologies, USA). The P–E loops are measured by applying a triangular wave of electric field with frequency of 1 Hz on the samples at room-temperature. The write/read tests are conducted by applying some self-defined waveforms of electric field on the samples at room-temperature. The dielectric property was measured by an LCR meter (TH 2818, Tonghui Technologies Inc., China). The piezoelectric constant d_{33} was measured by a quasi-static piezoelectric d_{33} meter (ZJ-3A, Institute of Acoustics, Chinese Academy of Sciences, China).

3 Results and discussion

3.1. Structural characterization

Fig. 1 shows the cross-sectional FESEM images of BNKT:xEu. All the samples display highly dense microstructure with neglectable pores. Besides, all elements are homogeneously distributed, as no element enrichment or deficiency is detected in grains or at the grain boundaries, according to the micro-compositional EDS analysis (Fig. S1†). Moreover, the quantitatively elements analysis by ICP and AAS (Table S1†) shows that the compositions of the samples are consistent with the design. The measurement results of bulk density show that all as-prepared samples present high relative densities, over 97% of the theoretical values (Table S2†). All these results indicate that the BNKT:xEu samples were well sintered.

Analysis of phase structure is conducted based on the XRD patterns measured from the ceramic powders. As displayed in Fig. 2(a), all the samples exhibit a perovskite phase, and no secondary phase is detected. Besides, the locally magnified patterns in Fig. 2(b) show that the (111) and (200) diffraction peaks are sharp and narrow, with no peak splitting, suggesting that the long-range general structure of the samples is very close to cubic. It should be noted that the samples used for XRD measurement are unpoled, and the near-cubic general structures are common observations in BNT-based materials, which is consistent with the fact that the BNT-based materials are usually in relaxor state before any electric field applied. Moreover, with the increasing of Eu^{3+} content, the diffraction peaks gradually shift to higher angles, illustrating a lattice shrink behavior according to the Bragg equation. This can be attributed to the smaller radius of Eu^{3+} (R_{Eu}^{3+} (12) = 1.30 Å)[32] (the number in bracket represents the coordination number)
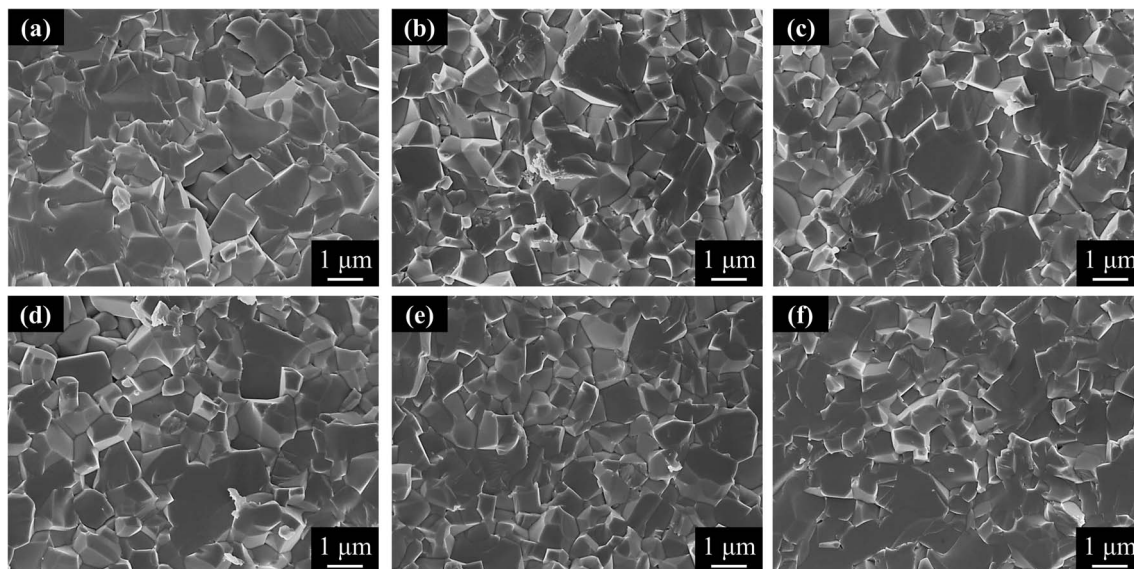
Fig. 1 FESEM images of the cross-sections of the as-prepared BNKT:xEu: (a) x = 0.0%, (b) x = 1.0%, (c) x = 2.0%, (d) x = 3.0%, (e) x = 4.0%, (f) x = 5.0%.
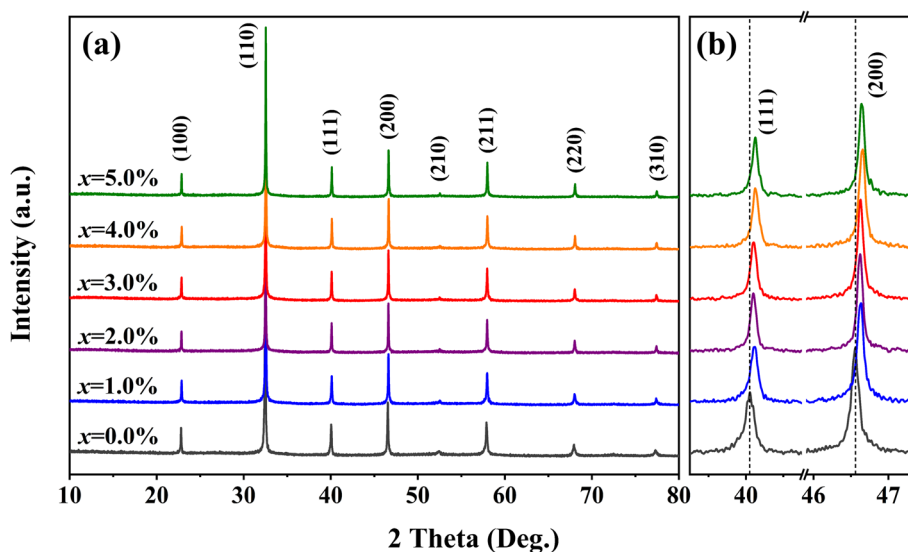

Fig. 2 (a) XRD patterns of BNKT:xEu ceramic powders; (b) the locally magnified in the range of $2\theta = 38.6-47.4°$.

compared with the average radius of A-site ($R_{Bi^{3+}}$ (12) = 1.38 Å, R_{Na^+} (12) = 1.39 Å, R_{K^+} (12) = 1.64 Å)[33,34] that it entered. Furthermore, the XPS results also support that the Eu^{3+} entered the A-site and substitute the Bi^{3+} (Fig. S2 and S3†).

3.2. Effect of Eu^{3+} doping on the local structure of BNKT

To figure out the effect of Eu^{3+} doping on the phase structure of BNKT, the XRD patterns of samples before and after poling are conducted, and the typical peaks in the range $2\theta = 39.0-47.5°$ are exhibited in Fig. 3. Before poling, all the samples exhibit predominately pseudo-cubic structures. This pseudo-cubic feature does not mean that there is no structural distortion in the sample, but implies the correlation length of the local

structural distortion is too small to be detected by XRD.[35] It is noted that there is a weak splitting of (11$\bar{1}$) diffraction peak for pure BNKT, which isn't exist in powder sample (Fig. 2(b)). This may be attributed to the slightly relaxor-to-ferroelectric transition induced by internal stress in plate samples.[36,37] Beyond that, all the Eu^{3+}-containing samples show no splitting of (11$\bar{1}$) and (200) diffraction peaks, which implies the inhibiting effect of Eu^{3+} for ferroelectric long-range texture, and the differences among the samples are negligible. After poling, the PNRs are transformed into ferroelectric domains, during which the correlation length of the local structural distortion increases and exceed the detect limit of XRD,[38] so the differences among various samples become distinct in XRD patterns. For pure
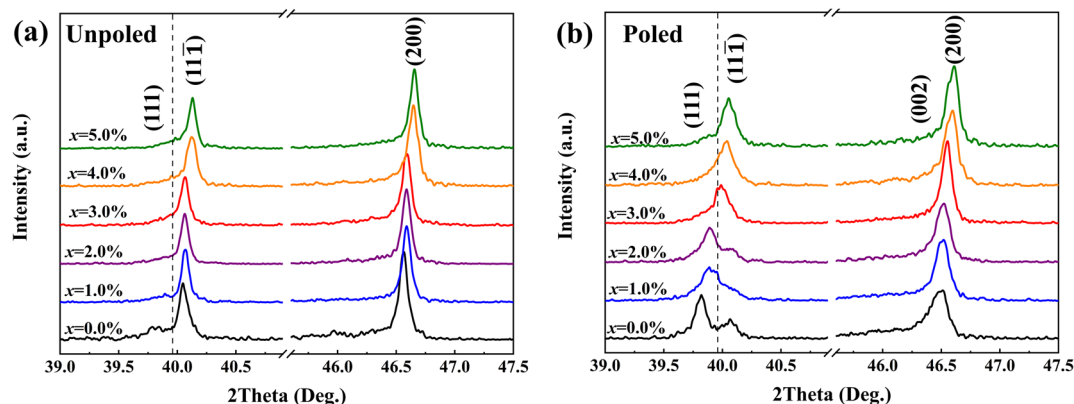
Fig. 3 XRD patterns of BNKT:xEu ceramics: (a) unpoled; (b) poled.

BNKT, there is a weak splitting of the (002)/(200) and a pronounced splitting of the (111)/(11$\bar{1}$) diffraction peaks, which indicates the coexistence of tetragonal phase (T phase) and rhombohedral phase (R phase). The intensity of (111) diffraction peak is higher than that of (11$\bar{1}$), suggesting that the R phase with a higher degree of structural distortion is predominant. However, with the increase of Eu^{3+} content, the intensity of (11$\bar{1}$) diffraction peak increases while the intensity

of (111) diffraction peak gradually decreases, and these two peaks gradually merge together. This result suggests that the structural changes induced by poling become more difficult to survive with the increase of Eu^{3+} content, which shows the destabilizing effect of Eu^{3+} doping on the electric field-induced ferroelectric state from a structural perspective.

The luminescence property of the rare earth Eu^{3+} ions and its sensitivity to local structural symmetry allow us to investigate
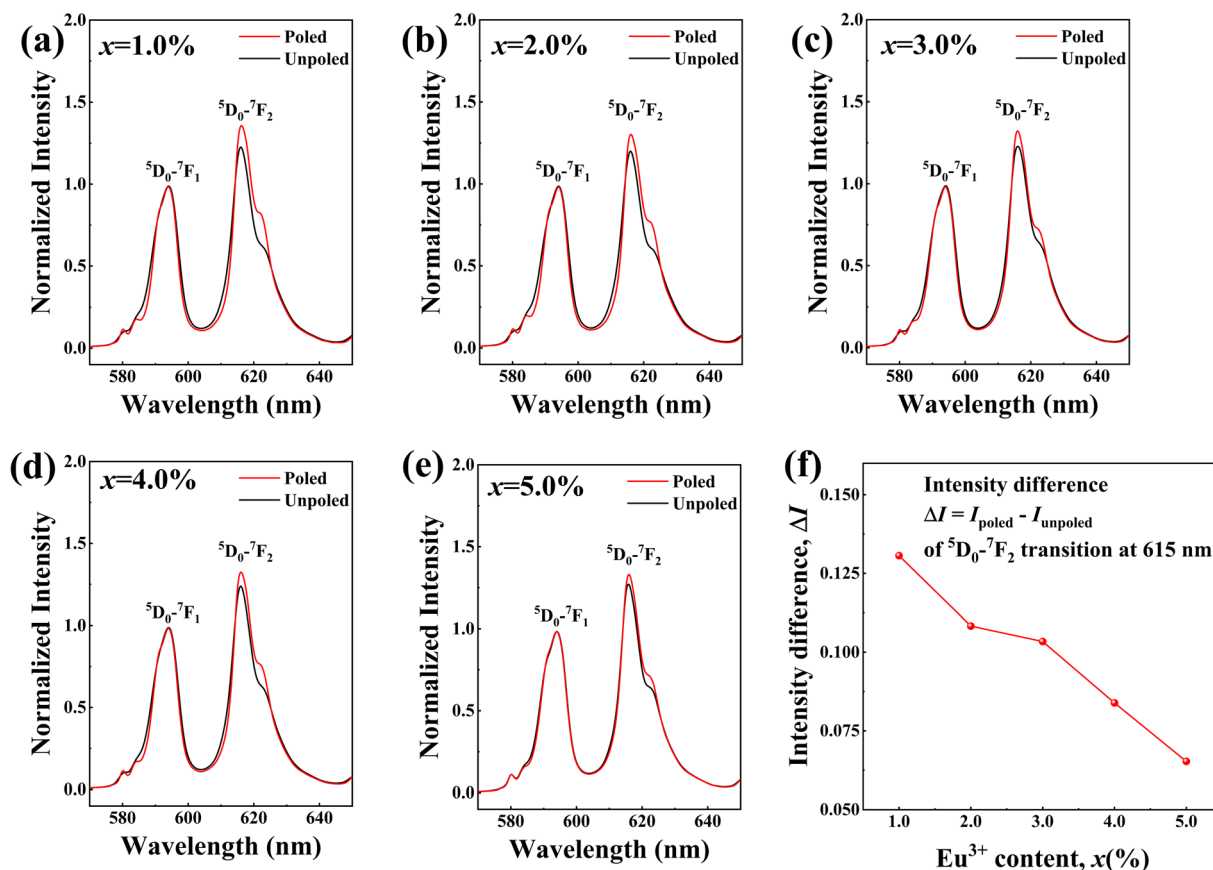

Fig. 4 The PL emission spectra of BNKT:xEu before and after poling, upon excitation at 465 nm: (a) $x = 1.0\%$; (b) $x = 2.0\%$; (c) $x = 3.0\%$; (d) $x = 4.0\%$; (e) $x = 5.0\%$. The intensity of the $^5D_0 \rightarrow \ ^7F_1$ peak is normalized to 1; (f) the difference of normalized intensity values of the $^5D_0 \rightarrow \ ^7F_2$ peak between the unpoled and poled samples.

the effect Eu^{3+} doping on the local structure by means of PL spectroscopy. Here, the laser with a wavelength of 465 nm is chosen to excite the Eu^{3+} because it shows the highest efficiency to excite the main emission peak around 615 nm (Fig. S4†). As shown in Fig. 4(a)–(e), when excited by the 465 nm laser beam, there are two obvious emission peaks in the range of 580–600 nm and 600–630 nm. The former emission peak around 592 nm is attributed to the $^5D_0 \rightarrow {}^7F_1$ transition, which is a magnetic dipole transition and independent of the local symmetry. The latter emission peak around 615 nm is categorized as the $^5D_0 \rightarrow {}^7F_2$ transition, which is an electric dipole transition and can be significantly affected by the distortion of local surroundings.[27,39] Therefore, the emission intensity ratio of the $^5D_0 \rightarrow {}^7F_2$ transition to the $^5D_0 \rightarrow {}^7F_1$ transition can be served as a probe to detect the local symmetry changes, so in this case, the intensity of the $^5D_0 \rightarrow {}^7F_1$ peak is normalized to 1. There is a common characteristic for all the samples: The intensity of the peak at 615 nm is higher in the poled state than that in the unpoled state. This is because when the samples are poled, a long-range dipole order is established, which is corresponding to higher structural asymmetry.[28,29] However, it is worth noting that, as shown in Fig. 4(f), the difference of the normalized intensity of the $^5D_0 \rightarrow {}^7F_2$ peak between poled and unpoled states continuously decreases as the Eu^{3+} content increases. This means that the poling-induced local asymmetry, as well as the long-range ferroelectric order, becomes more difficult to establish. The results of PL spectra, on the one hand,

show the capability of the Eu^{3+} ion to be a probe of local structural symmetry, and on the other hand, also demonstrate that the doping of Eu^{3+} in BNKT tends to enhance the local structural disorder and weaken the stability of electric field-induced long-range ferroelectric order.

3.3. Effect of Eu^{3+} doping on the ferroelectric behavior of BNKT

Ferroelectric polarization switching behavior of the BNKT:xEu is characterized by $P–E$ loops and $J–E$ curves, as shown in Fig. 5. With the increasing of Eu^{3+} content, the $P–E$ loop gradually becomes narrower (Fig. 5(a)). From the $P–E$ loop, we can extract two valuable physical parameters, P_s and P_r. Generally, the saturated polarization P_s is mainly contributed by the long-range orderly aligned dipoles under electric field, while the remnant polarization P_r represents the remanence of the dipoles after removal of electric field. As exhibited in Fig. 5(b), both P_s and P_r show a slightly increase incipiently, after reaching a peak at $x = 2.0\%$, a decline is then observed with further increase of Eu^{3+} content. It is noted that the decline in P_r is more pronounced than the decline of P_s. This phenomenon suggests that when excessive Eu^{3+} is doped (3% or more), the electric field-induced ferroelectric state with long-range dipole order becomes less stable, and the sample would partially reverse back to the original ergodic relaxor state during the removal of electric field.
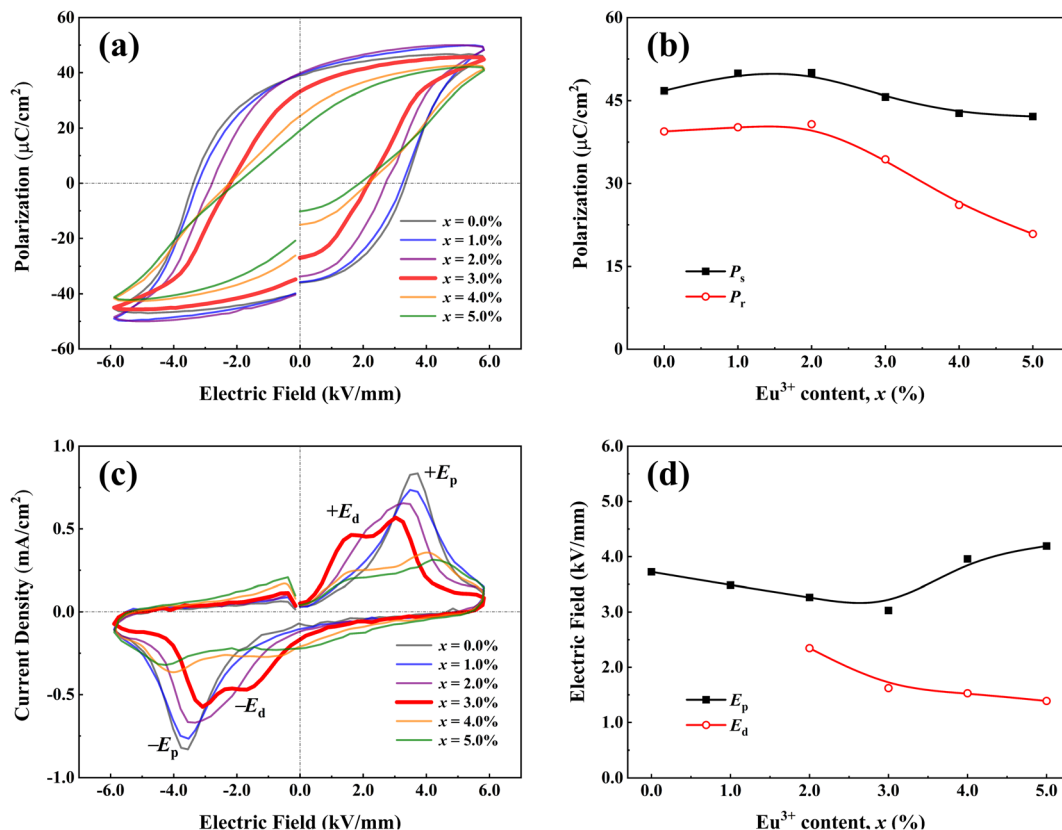

Fig. 5 (a) $P–E$ hysteresis loops of BNKT:xEu; (b) P_s and P_r as a function of Eu^{3+} content; (c) $J–E$ curves of BNKT:xEu; (d) E_p and E_d as a function of Eu^{3+} content.

More detailed information on the changes of polarization state during the electrical cycles can be read from the J–E curves, where the current density J is calculated by taking the first-order derivative of the polarization P with respect to time. As can be seen in Fig. 5(c), there is only one pair of sharp peaks at $\pm E_p$ for BNKT:0.0%Eu and BNKT:1.0%Eu, indicating that the samples are directly switched between the two ferroelectric states with upward and downward polarizations at coercive field. In comparison, for the BNKT:2.0%Eu and BNKT:3.0%Eu, an additional pair of current density peaks appears at $\pm E_d$ in the lower electric field region, suggesting that the relaxor state appears during the electrical cycle. The occurrence of the relaxor state is a result of disruption of long-range ferroelectric order by Eu^{3+} doping. When the Eu^{3+} content is further increased, all the current peaks become more diffused, and the peaks at $\pm E_p$ move to higher field while the peaks at $\pm E_d$ toward the opposite direction (Fig. 5(d)). This phenomenon indicates that the process of the relaxor-to-ferroelectric transition under the electric field is further hindered, and the electric field-induced ferroelectric state is more unstable when the Eu^{3+} content is relatively high. In brief, the results of P–E loops and J–E curves reveal that the introducing of Eu^{3+} is capable to tailor the ferroelectric behavior in BNKT. With the Eu^{3+} doping, the electric field-induced ferroelectric order is gradually destabilized, and the disordered relaxor state in BNKT is more favored than the ferroelectric state with long-range orders.

The effect of Eu^{3+} doping on the ferroelectric behavior is also manifested in the dielectric and piezoelectric properties. Fig. S5† shows the relative dielectric constant $\varepsilon_{33}/\varepsilon_0$ and the piezoelectric constant d_{33} of BNKTs. For a given Eu^{3+} doping content, the dielectric constant after poling is smaller than that before poling. This can be explained by the development of long-range ferroelectric order during the poling treatment. The dynamic nature and the response to electric field are lower for the macro-domains in the poled samples than the polar regions with smaller sizes in the unpoled samples. However, the difference of dielectric constants between before-poling state and after-poling state becomes smaller when the Eu^{3+} content is increased. This shows the development of long-range ferroelectric orders by the poling process becomes more difficult when the sample contains high content of Eu^{3+}. In addition, it can be seen from Fig. S5† that with the increase of Eu^{3+} content,

the $\varepsilon_{33}/\varepsilon_0$ after poling is almost unchanged, while the d_{33} shows a continuous decrease. According to the formula $d_{33} = 2Q\varepsilon_{33}P_r$ predicted by the Landau–Devonshire phenomenological theory, where Q is the electrostrictive coefficient and insensitive to chemical modifications,[40] it is clear that the decrease of d_{33} with Eu^{3+} doping is closely related to the decrease of P_r, and therefore, the destabilization of ferroelectric order induced by Eu^{3+} doping is further verified.

3.4. Tristate ferroelectric memory effect in Eu^{3+} doped BNKT

In the previous section, we have demonstrated that the Eu^{3+} doping is capable to continuous tune the ferroelectric behavior of BNKT. With the increase of Eu^{3+} content, the long-range ferroelectric order is gradually destabilized, and the P–E loops gradually become pinched and double-like, indicating that an intermediate relaxor state appears during the polarization reversal. In the following, we turn to focus on a specific composition in the series of the samples, the BNKT:3.0%Eu. This composition possesses the split current density peaks in J–E curve, along with a slightly pinched P–E loop in which the remnant polarization is well kept. Such a ferroelectric behavior implies the possibility for tristate ferroelectric memory.[13,41–43] We provide experimental verification of this novel memory effect on BNKT:3.0%Eu in this section.

Fig. 6 illustrates the principle of the tristate ferroelectric memory effect. For explicitly, we idealize the slightly pinched P–E loop of the BNKT:3.0%Eu and depicted in Fig. 6(a). This kind of P–E loop is a typical result of triple-well free energy landscape, as schematically shown in Fig. 6(b). As shown, three polarization states, including the relaxor state (RE) and two ferroelectric states (the ferroelectric states with upward and downward polarization are denoted as FE(+) and FE(−), respectively) can stably existed when the electric field is unloaded. Therefore, the RE, FE(+) and FE(−) states could be served as the "0", "+1" and "−1" digits for non-volatile memory. Moreover, the polarization state can be switched among all these three states by electric field. This provides the basis for data writing and reading. We designed three kinds of electric field waveforms to write these three states (Fig. 7). The write of "+1" is operated by applying a sufficiently large positive trapezoidal pulse to redress any initial state to the FE(+) state, and analogously, the write of "−1" is operated by
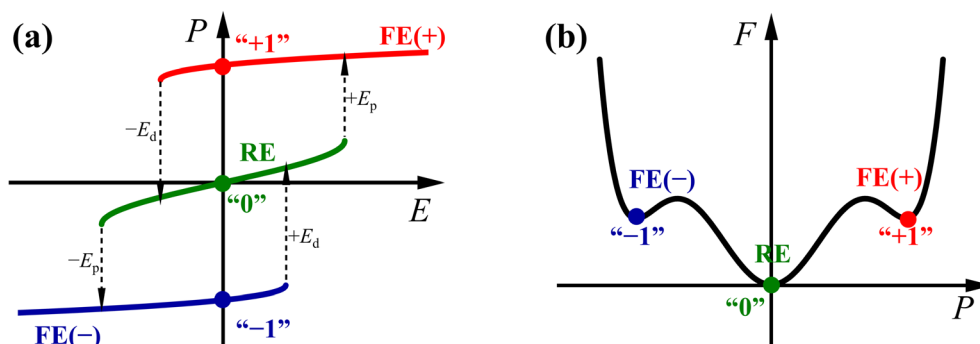

Fig. 6 (a) Ideal double-like P–E loop for tristate ferroelectric memory; (b) free energy density curve of the triple-well free energy landscape.
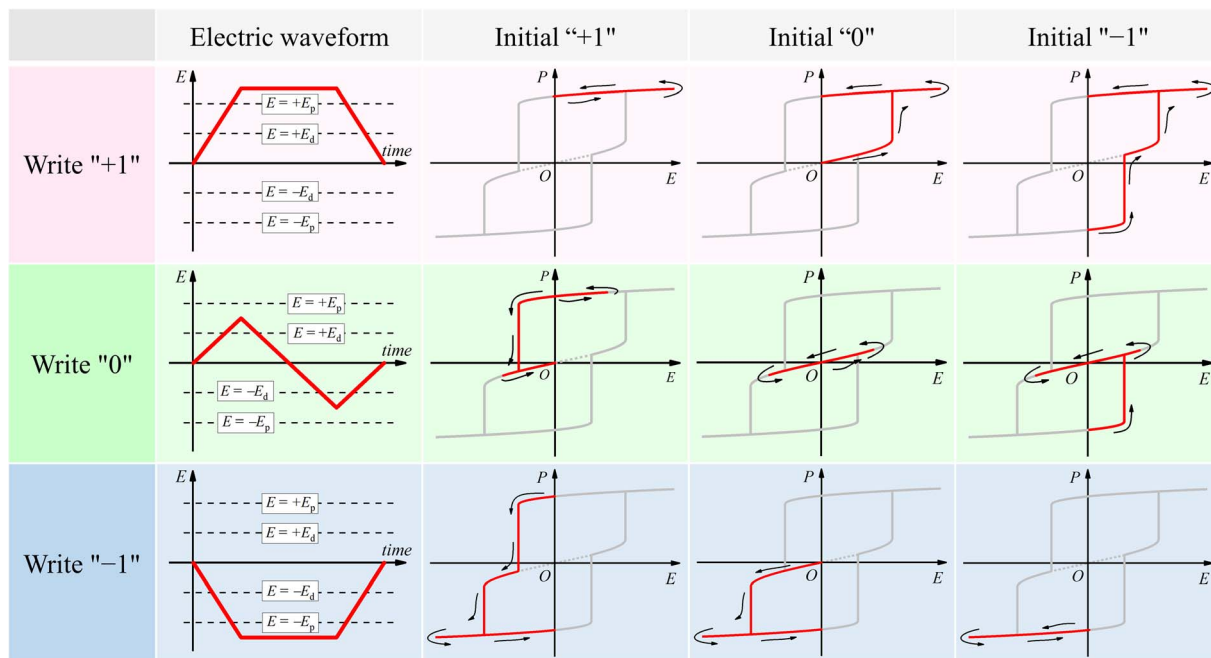
Fig. 7 Schematics of electric field waveforms for writing "+1", "0" and "−1" and the corresponding polarization changes during the writing from different initial states.

applying a sufficiently large negative trapezoidal pulse to redress any initial state to the FE(−) state. We herein highlight the write of "0", which is operated by applying a bipolar triangular waveform with the amplitude between E_d and E_p. As illustrated in Fig. 7, such a bipolar triangular waveform is capable to transform whatever initial state to the RE state.
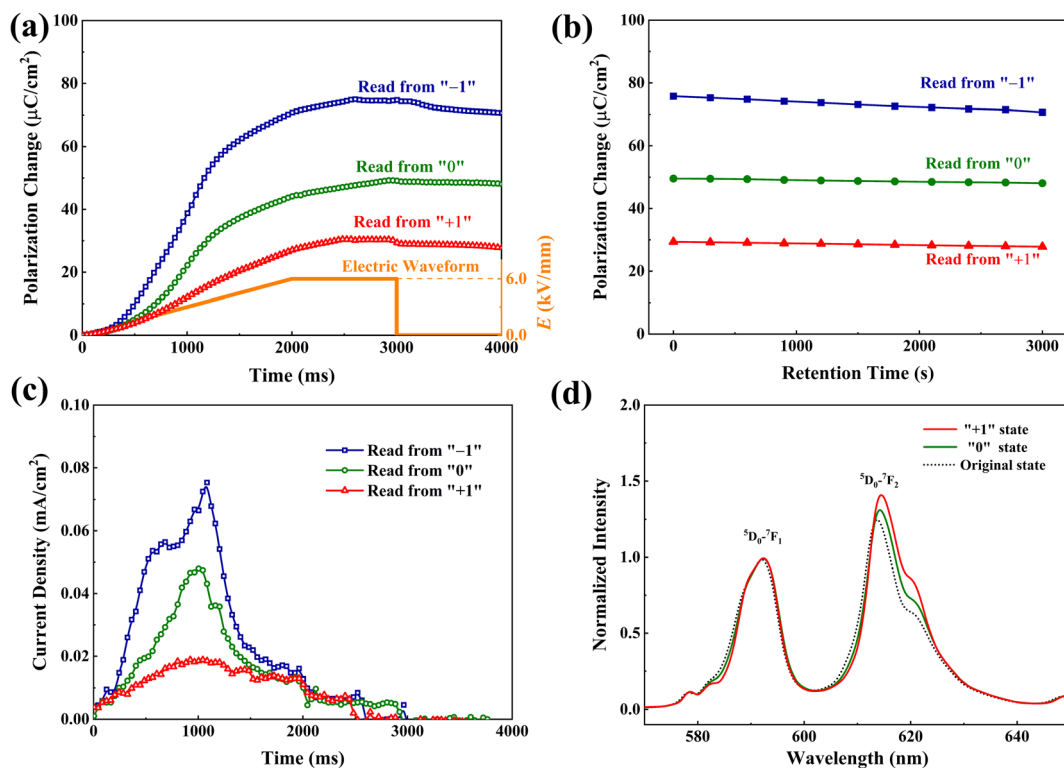

Fig. 8 Experimental verification of tristate ferroelectric memory effect in BNKT:3.0%Eu. (a) Electric field waveform and the polarization changes during the reading from "+1", "0" and "−1"; (b) the retention test; (c) current density during the reading process; (d) PL spectra measured from different written states and the un-written original state.

Fig. 8 shows the experimental verification of tristate ferroelectric memory effect in BNKT:3.0%Eu. We use the aforementioned waveforms to write different states (the amplitudes of electric waveforms are ± 5.0 kV mm^{-1} for writing "± 1" and 2.5 kV mm^{-1} for writing "0", see details in Fig. S6†), and then read each written state and record the polarization change during the reading process (the read operation is to apply a positive trapezoidal pulse of 6.0 kV mm^{-1}, see also in Fig. S6†). As shown in Fig. 8(a), samples in different written states would experience different polarization changes ΔP, and this would be the reflection of different written states. The results in Fig. 8(a) prove that the tristate ferroelectric memory effect can be realized in BNKT:3.0%Eu, i.e. the write and read of "0", "+1" and "−1" are all feasible. Moreover, from a performance point of view, ΔP values from different written states are well separated by margins of approximately 20 μC cm^{-2}, which is large enough to avoid misreading. In addition, we investigated the retention ability of the tristate ferroelectric memory in BNKT:3.0%Eu. As shown in Fig. 8(b), the value of ΔP keeps almost unchanged up to a retention time of 3000 s, which suggests that all the three states are fairly stable. Therefore, the retention ability of the tristate ferroelectric memory in BNKT:3.0%Eu is reasonably good. We also conducted a 10 days test of repeatedly doing write and read operation once every 12 h. The results do not reveal any significant performance changes, which demonstrates the repeatability and long-term stability of the memory effect (Fig. S7†).

To inspect whether the "0", "+1" and "−1" written states are indeed predominately the RE, FE(+) and FE(−), respectively, we calculated the current density during the reading process, shown in Fig. 8(c). As seen, the current density curves reading from different states are completely different. Particularly, the curves have different number of current density peaks. For the J–E curve read from the "+1" state, there is no current density peak, suggesting that no phase transition occurs, and thus the "+1" state is predominately FE(+). As for the J–E curve read from "0" state, one current density peak can be observed, which results from the RE to FE(+) transition, so the "0" state is predominately RE. Moreover, there are two current density peaks when read from "−1", suggesting the two successive transitions from FE(−) to RE and then to FE(+), and therefore, the "−1" state is predominately FE(−). The working mechanism of the tristate ferroelectric memory follows exactly the principle as proposed.

Furthermore, we investigated the phase structure of different written state from a structural perspective. Fig. 8(d) compares the PL spectra measured from different written states and the un-written original state, where the intensity of the $^5D_0 \rightarrow {}^7F_1$ emission peak is normalized to 1. As seen, the pre-written "+1" state shows a distinct enhancement of emission intensity of the $^5D_0 \rightarrow {}^7F_2$ transition compared with the un-written original state, indicating that the pre-written "+1" state locally has a high asymmetry feature and therefore is corresponding to the polarized FE state (the same for "−1" state by analogy). For "0" state, the emission intensity of the $^5D_0 \rightarrow {}^7F_2$ transition is much weaker than that of the "+1" state and closer to that of un-written original state, showing that the local surrounding of

Eu^{3+} is relatively symmetrical, which is related to the locally disordered RE state. Moreover, the PL results are further verified by the XRD Rietveld refinement (Fig. S8†). As known, R phase and T phase are coexisted in the BNKT:3.0%Eu. The R phase with more distorted phase structure accounts for 69.30% in the "+1" state (approximate in the "−1" state), owing to the electric field-induced ferroelectric orders in FE state. While the volume fraction of R phase when sample is in "0" state is calculated to be only 54.80%, corresponding to lower local asymmetry in the RE state. Therefore, it is convincing that the three states are with different degree of structure distortion, and the PL spectra is more convenient to understand the structural changes related to the different memory states compared with the XRD Rietveld refinements, which requires strict high-quality XRD data and time-consuming calculating.

Moreover, the different photoluminescent features of different written states may be further utilized to distinguish the "0" and "±1", which implies a potential possibility to design a novel scheme of nondestructive optical readout.

4   Conclusions

In summary, the effects of Eu^{3+} doping on the local structure and ferroelectric behavior of BNKT are investigated by structural characterization and electrical properties. The addition of Eu^{3+} in BNKT tends to enhance the local structural disorder and weaken the stability of electric field-induced long-range ferroelectric order. In the series of Eu^{3+} doped BNKT samples, the BNKT:3.0%Eu with a slightly pinched P–E loop is found to be suitable for tristate ferroelectric memory effect. The write/read operation and retention test show the feasibility and stability of it. The working mechanism and principle of the tristate ferroelectric memory are illustrated thoroughly. The luminescence property of Eu^{3+}, owning to its sensitivity to local structural symmetry, offers an original way to understand the structural changes related to the switching of the memory states and also provides the potential for non-destructive optical readout.

Conflicts of interest

The authors declare no competing financial interests.

Acknowledgements

References

1 T. Zheng, J. Wu, D. Xiao and J. Zhu, Prog. Mater. Sci., 2018, 98, 552–624.

2   L. Yang, X. Kong, F. Li, H. Hao, Z. Cheng, H. Liu, J. Li and S. Zhang, *Prog. Mater. Sci.*, 2019, **102**, 72–108.

3   J. Wu, *J. Appl. Phys.*, 2020, **127**, 190901.

4   X. Zhou, G. Xue, H. Luo, C. R. Bowen and D. Zhang, *Prog. Mater. Sci.*, 2021, **122**, 100836.

5   E. Aksel, J. S. Forrester, J. C. Nino, K. Page, D. P. Shoemaker and J. L. Jones, *Phys. Rev. B: Condens. Matter Mater. Phys.*, 2013, **87**, 104113.

6   X. Lv, X. Zhang and J. Wu, *J. Mater. Chem. A*, 2020, **8**, 10026–10073.

7   J. Han, J. Yin and J. Wu, *J. Eur. Ceram. Soc.*, 2020, **40**, 5392–5401.

8   X. Liu and X. Tan, *Adv. Mater.*, 2016, **28**, 574–578.

9   G. Li, J. Li, F. Li, Y. Li, X. Liu, T. Jiang, F. Yan, X. He, B. Shen and J. Zhai, *J. Alloys Compd.*, 2020, **817**, 152794.

10 J. Zhang, Y. Lin, L. Wang, Y. Yang, H. Yang and Q. Yuan, *J. Eur. Ceram. Soc.*, 2020, **40**, 5458–5465.

11 M. Li, M. J. Pietrowski, R. A. De Souza, H. Zhang, I. M. Reaney, S. N. Cook, J. A. Kilner and D. C. Sinclair, *Nat. Mater.*, 2014, **13**, 31–35.

12 M. Lun, W. Wang, Z. Xing, Z. Wan, W. Wu, H. Song, Y. Wang, W. Li, B. Chu and Q. He, *J. Am. Ceram. Soc.*, 2019, **102**, 5243–5252.

13 H. Zhang, J. Zhou, J. Shen, T. Wang, D. Xie and W. Chen, *Appl. Phys. Lett.*, 2018, **113**, 152902.

14 J. Zhang, R. X. Wang, L. Li, J. Y. Wu, Y. S. Cui, Z. B. Gu, H. Zhang, M. W. Zhu, S. T. Zhang and B. Yang, *J. Eur. Ceram. Soc.*, 2019, **39**, 4705–4711.

15 P. Shi, X. Zhu, X. Lou, B. Yang, Q. Liu, C. Kong, S. Yang, L. He, R. Kang and J. Zhao, *Chem. Eng. J.*, 2022, **428**, 132612.

16 Y. Zhang, G. Liang, S. Tang, B. Peng, Q. Zhang, L. Liu and W. Sun, *Ceram. Int.*, 2020, **46**, 1343–1351.

17 H. Z. Zhang, J. Zhou, J. Shen, X. Yang, C. L. Wu, K. K. Han, Z. H. Zhao and W. Chen, *Ceram. Int.*, 2017, **43**, 16395–16402.

18 Y. Si, Y. Li, L. Li, H. Li, Z. Zhao and Y. Dai, *J. Am. Ceram. Soc.*, 2019, **103**, 1765–1772.

19 J. Zhang, Z. Pan, F. F. Guo, W. C. Liu, H. Ning, Y. B. Chen, M. H. Lu, B. Yang, J. Chen, S. T. Zhang, X. Xing, J. Rodel, W. Cao and Y. F. Chen, *Nat. Commun.*, 2015, **6**, 6615.

20 J. Yin, Y. Wang, Y. Zhang, B. Wu and J. Wu, *Acta Mater.*, 2018, **158**, 269–277.

21 C. Groh, D. J. Franzbach, W. Jo, K. G. Webber, J. Kling, L. A. Schmitt, H. J. Kleebe, S. J. Jeong, J. S. Lee and J. Rödel, *Adv. Funct. Mater.*, 2014, **24**, 356–362.

22 F. Li, M. J. Cabral, B. Xu, Z. Cheng, E. C. Dickey, J. M. LeBeau, J. Wang, J. Luo, S. Taylor, W. Hackenberger, L. Bellaiche, Z. Xu, L. Q. Chen, T. R. Shrout and S. Zhang, *Science*, 2019, **364**, 264–268.

23 F. Li, S. Zhang, D. Damjanovic, L. Q. Chen and T. R. Shrout, *Adv. Funct. Mater.*, 2018, **28**, 1801504.

24 C. Ma, X. Wang, W. Tan, W. Zhou, X. Wang, Z. Cheng, G. Chen and Z. Zhai, *Dalton Trans.*, 2020, **49**, 5581–5589.

25 X. Wu, T. H. Chung, H. Sun and K. W. Kwok, *Ceram. Int.*, 2016, **42**, 9899–9905.

26 B. Jvud, *Phys. Rev.*, 1962, **127**, 750–761.

27 K. Binnemans, *Coord. Chem. Rev.*, 2015, **295**, 1–45.

28 L. Zeng and J. Zhou, *J. Am. Ceram. Soc.*, 2019, **103**, 2296–2301.

29 P. Du, L. Luo, W. Li, Y. Zhang and H. Chen, *J. Alloys Compd.*, 2013, **559**, 92–96.

30 J. Cao, L. Li, L. Wang, X. Li, Z. Zhang, S. Xu and M. Peng, *J. Mater. Chem. C*, 2018, **6**, 5384–5390.

31 S. Said, P. Marchet, T. Merle Mejean and J. P. Mercurio, *Mater. Lett.*, 2004, **58**, 1405–1409.

32 G. P. Espinosa, *J. Chem. Phys.*, 1962, **37**, 2344–2347.

33 R. D. Shannon, *Acta Crystallogr., Sect. A: Cryst. Phys., Diffr., Theor. Gen. Crystallogr.*, 1976, **32**, 751–767.

34 C. Long and H. Fan, *Dalton Trans.*, 2012, **41**, 11046–11054.

35 A. R. Paterson, H. Nagata, X. Tan, J. E. Daniels, M. Hinterstein, R. Ranjan, P. B. Groszewicz, W. Jo and J. L. Jones, *MRS Bull.*, 2018, **43**, 600–606.

36 R. Garg, B. N. Rao, A. Senyshyn, P. S. R. Krishna and R. Ranjan, *Phys. Rev. B: Condens. Matter Mater. Phys.*, 2013, **88**, 014103.

37 F. H. Schader, Z. Wang, M. Hinterstein, J. E. Daniels and K. G. Webber, *Phys. Rev. B*, 2016, **93**, 134111.

38 X. Liu, J. Zhai and B. Shen, *J. Am. Ceram. Soc.*, 2018, **101**, 5604–5614.

39 C. Görller Walrand, L. Fluyt, A. Ceulemans and W. T. Carnall, *J. Chem. Phys.*, 1991, **95**, 3099–3106.

40 F. Li, L. Jin, Z. Xu and S. Zhang, *Appl. Phys. Rev.*, 2014, **1**, 011103.

41 G. A. Boni, L. D. Filip, C. Chirila, I. Pasuk, R. Negrea, I. Pintilie and L. Pintilie, *Nanoscale*, 2017, **9**, 19271–19278.

42 S. Saremi, R. J. Xu, F. I. Allen, J. Maher, J. C. Agar, R. Gao, P. Hosemann and L. W. Martin, *Phys. Rev. Mater.*, 2018, **2**, 084414.

43 P. F. Hou, C. Chen, B. Li, S. Z. Zheng, J. B. Wang, X. L. Zhong and M. Liao, *Adv. Funct. Mater.*, 2021, **31**, 2011029.